ADVANCED THEORY AND SIMULATIONS
www.advtheorysimul.com

Optical Simulations of Nanotextured All-Perovskite Tandem Solar Cells

Klaus Jäger, Alvaro Tejada, Sebastian Berwig, Martin Hammerschmidt, Philipp Tockhorn, Steve Albrecht, and Christiane Becker**

This numerical study investigates, how textures at various locations of all-perovskite tandem solar cells affect their optical performance. For this, hexagonal sinusoidal textures with 750 nm period and aspect ratios (height-to-period) of 27% (moderate) and 54% (pronounced) are considered. The optical simulations are performed with the finite element method and an algorithm to correct for the thick glass superstrate. The complex refractive index data of the wide-bandgap (WBG) and narrow-bandgap (NBG) perovskites with spectroscopic ellipsometry is determined. Texturing between the glass superstrate and the WBG perovskite top cell has an antireflective effect across the whole wavelength region. In contrast, texturing between the WBG perovskite top cell and the NBG perovskite bottom cell has no additional effect for a moderate texture but leads to light trapping in the NBG perovskite for a pronounced texture. Moderate texturing between the NBG perovskite absorber and the metal back contact leads to light trapping in the NBG perovskite but also excites surface plasmons in the copper back contact. Dielectric interlayers between the NBG perovskite and the metal back contact can reduce the plasmonic absorption losses. Texturing potentially allows to increase the current-matched short-circuit current density beyond 17 mA cm^{-2}.

1. Introduction

Of all energy technologies, solar and wind power have the largest potential to reduce greenhouse gas emissions, as pointed out in the latest synthesis report from the International Panel on Climate Change.[1] Currently, photovoltaic solar energy relies mostly on silicon solar cells, where the power conversion efficiency (PCE) is theoretically limited to 29.4%.[2]

In multi-junction solar cells, several solar cells with different bandgaps are stacked onto each other to better utilize the energy of the solar spectrum and to surpass single-junction PCE limit. Amongst the promising concepts are perovskite/silicon tandem solar cells in which a perovskite solar cell is manufactured atop a silicon solar cell. The perovskite top cell has a higher bandgap energy ($E_g \approx 1.7$ eV) than the silicon bottom cell ($E_g = 1.12$ eV), which decreases the thermalization losses and leads to an increased PCE. This concept enabled tremendous progress in recent years with a current PCE record of 34.6 %.[3] It was shown that light management through—amongst others—texturing improves the performance of perovskite/silicon tandem solar cells.[4–8]

Recently, all-perovskite tandem solar cells (APTSC) attracted broad attention because they promise high PCEs and a cost-effective fabrication on light-weight, flexible substrates, and a low carbon dioxide footprint.[9–11] PCEs of 28.8%[12] and even

K. Jäger, C. Becker
Dept. Optics for Solar Energy
Helmholtz-Zentrum Berlin für Materialien und Energie
Kekuléstraße 5, 12489 Berlin, Germany
E-mail: klaus.jaeger@helmholtz-berlin.de; christiane.becker@helmholtz-berlin.de

K. Jäger, M. Hammerschmidt
Computational Nanooptics
Zuse Institute Berlin
Takustraße 7, 14195 Berlin, Germany

A. Tejada
Departamento de Ciencias, Sección Física
Pontificia Universidad Católica del Perú
Av. Universitaria 1801, Lima 15088, Peru

S. Berwig, P. Tockhorn, S. Albrecht
Department Perovskite Tandem Solar Cells
Helmholtz-Zentrum Berlin für Materialien und Energie
Kekuléstraße 5, 12489 Berlin, Germany

M. Hammerschmidt
JCMwave GmbH
Bolivarallee 22, 14050 Berlin, Germany

S. Albrecht
Faculty IV – Electrical Engineering and Computer Science
Technische Universität Berlin
Marchstraße 23, 10587 Berlin, Germany

C. Becker
Faculty 1: School of Engineering – Energy and Information
Hochschule für Technik und Wirtschaft Berlin
Wilhelminenhofstraße 75A, 12459 Berlin, Germany

The ORCID identification number(s) for the author(s) of this article can be found under https://doi.org/10.1002/adts.202400724

DOI: 10.1002/adts.202400724

29.1%[13,14] were reported. So far, most reported APTSCs employ a planar layer geometry and are not fully optimized from an optical point of view. For the top cell, usually wide bandgap (WBG) lead-based perovskites ($E_g \approx 1.8$ eV) and for the bottom cells, usually narrow bandgap (NBG) lead-tin (Pb–Sn) hybrid perovskites ($E_g \approx 1.24$ eV) are used. For the typical B-site anions Sn and Pb, the minimum bandgap is constrained through an anomalous bowing effect.[15] Because the bandgap of the NBG perovskite is wider than that of silicon, the maximum achievable photogenerated current of APTSCs is lower than for silicon-based solar cells. This highlights the importance of light management to minimize optical losses. Moreover, the absorption onset of NBG perovskites tends to be weaker than for WBG perovskites, which requires thicker layers or path length enhancement, for example through scattering. So far, most reported APTSCs employ a planar layer geometry and are not fully optimized from an optical point of view. Only recently, the effect of texturing in all-perovskite tandem solar cells was investigated with simulations.[16] Further, optically enhanced NBG perovskite layers were experimentally shown using light scattering resin particles[17] or a textured hole-transporting layer based on tin oxide chloride.[18]

In this work, we present optical simulations of monolithic all-perovskite tandem solar cells. In particular, we study how sinusoidal nanotextures at different positions of the solar cell affect the optical performance. Sinusoidal nanotextures were shown to optically outperform inverted-pyramid and pillar textures for single-junction perovskite solar cells,[19] and showed an excellent optoelectronic performance in perovskite/silicon tandem solar cells, where they also increased the open-circuit voltage with respect to the planar reference Ref. [6]. For the optical simulations, we combine the finite element method with a newly developed rigorous "glass-correction algorithm" to account for the interaction of light with the air/glass interface of the thick glass superstrate.[20] At the beginning of this study, we discuss the derivation of the complex refractive index (*nk*) data of the WBG and NBG perovskites from spectroscopic ellipsometry measurements and we validate the *nk* data of the different layers by comparing results from optical simulations of APTSCs to experimental data. This work provides guidelines on how to further improve the performance of all-perovskite tandem solar cells using textured interfaces.

2. Optical Data

Accurate optical simulation of solar cells requires appropriate complex refractive index (*nk*) data. For the WBG perovskite, typically lead-based compositions with a bromine content of ≥ 30% are used. In this study, we use a WBG perovskite with the nominal composition $(Cs_{0.22}FA_{0.78}PbI_{2.1}Br_{0.9})_{0.9}(MAPbCl_3)_{0.1}$ and a bandgap of 1.8 eV, where FA and MA denote formamidinium and methylammonium, respectively. For the NBG perovskite, typical compositions have a Sn:Pb ratio of 50:50 and a pure iodine *X*-site. In this study, the nominal composition $Cs_{0.1}FA_{0.6}MA_{0.3}Sn_{0.5}Pb_{0.5}I_3$ with a bandgap of 1.24 eV is used. A literature survey of the reported *nk*-data for WBG and NBG perovskites (see Figure S2a, Supporting Information) shows that in particular the *k*-data in the band-edge regions of both, WBG and NBG perovskites, vary significantly amongst different studies.[21–24] Moreover, Figure S2 (Supporting Information) shows that the absorptivity of the NBG perovskite in the band-edge region is significantly lower than that of the WBG perovskite. This is compatible with a theoretical analysis by Filippetti and coworkers, who calculated a lower density of states near the band-edges for Sn-containing perovskites.[25] As a consequence, thicker layers of NBG perovskite are required, which may be challenging because of limiting carrier diffusion lengths as thick layers can reduce the collection efficiency.

For an accurate simulation of the band-edge region, it is important to use *nk* data that are not distorted by surface roughness in ellipsometry measurements. Therefore, we determined new datasets for WBG and NBG perovskites for this study. For this, perovskite films were deposited on fused silica substrates through spin coating, as described in the Supporting Information. These samples were characterized with a SENTECH SENResearch 4.0 spectroscopic ellipsometer in the range from 190 to 2500 nm at incidence angles of 50°, 60° and 70°.

Fits were performed with the SENTECH SpectraRay/4 software. Substrate backside reflections were considered in the optical models, as well as surface roughness at the air/perovskite interface. The root mean square (RMS) roughness layer was modeled with a Bruggemann Effective Medium Approximation (EMA),[26] and yielded RMS values below 7 nm for both perovskite compositions. Tauc–Lorentz oscillators[27,28] were used for the dispersion model, requiring ten oscillators for the WBG perovskite and seven for the NBG perovskite.

This procedure yielded *nk* spectra with non-negligible sub-bandgap absorption, which was likely due to the Bruggemann EMA being unable to completely account for the surface roughness.[26,29] This is a common challenge for not ideally flat thin films and requires further analysis efforts. To compensate for the effect of surface roughness, an additional correction procedure, which was previously described by Fujiwara,[29] was performed. For this correction, synthetic ellipsometry spectra (Ψ and Δ) were generated from the previously obtained complex refractive indices, assuming the optical model for a bulk material. These spectra were then fitted point-by-point, while iteratively assuming increasing levels of surface roughness. This was done until the sub-bandgap absorption became negligible, to within a roughness layer thickness variation step of 0.01 nm. The resulting complex refractive index spectra are shown in Figure S2b (Supporting Information).

To validate the optical data and to calibrate the layer thicknesses, we fabricated planar APTSCs and performed optical simulations of these solar cells. Then we compared simulated data to experimentally measured reflection and external quantum efficiency spectra. The solar cells were fabricated in superstrate configuration, similar to our previous publication.[30] The complete device structure of the APTSCs is as follows: onto a glass superstrate an transparent conducting oxide (TCO) of type "nSCOT" from ANP Corporation[31] is deposited, which constitutes the electric front contact; [2-(9H-Carbazol-9-yl)ethyl]phosphonic acid (2PACz) forms the hole transport self-assembled monolayer (SAM) for the top cell; buckminsterfullerene (C_{60}) and tin oxide form the (SnO_2) electron transport layers for both subcells; indium tin oxide (ITO) forms a recombination layer; poly(3,4-ethylenedioxythiophene) polystyrene sulfonate (PEDOT:PSS) forms the hole transport layer of the bottom cell; and copper forms the electric back contact. In summary, the

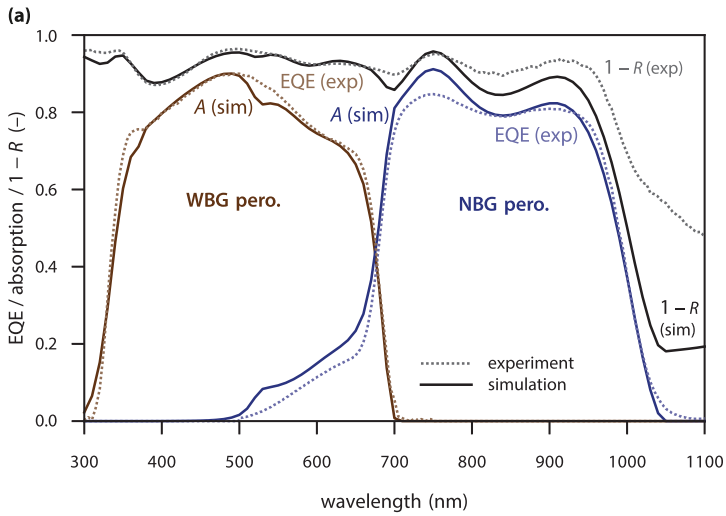

(b)

material	thickness (nm)
Glass	1.1 mm
front TCO	165
WBG pero	465
C_{60} / SnO_2	23/20
ITO	90
PEDOT:PSS	30
NBG pero	1000
C_{60} / SnO_2	23/20
copper	100

Figure 1. a) Measured external quantum efficiency (EQE) and $1 - R$ data (dashed lines) and simulated absorption and $1 - R$ data (full lines) of the all-perovskite tandem solar cell. b) Calibrated layer thicknesses used in the simulations.

layer stack is given as glass | front TCO | 2PACz | WBG perovskite | C_{60} | SnO_2 | ITO | PEDOT:PSS | NBG perovskite| C_{60} | SnO_2 | Cu. Further details of the fabrication process, as well as details on the external quantum efficiency (EQE) and reflectance measurements are given in the Supporting Information.

For this validation, we used the simulation package `GenPro4` that is based on the net-radiation method and can simulate layers with coherent and incoherent propagation of light as well as scattering using ray tracing.[32] Here, we used GenPro4 instead of the finite element method (FEM) package `JCMsuite` (see below) because `GenPro4` allows to combine the layers with coherent and incoherent propagation. However, it is not able to perform rigorous simulations of periodically nanotextured, which is the main focus of this paper.

For the simulation, we assumed incoherent light propagation in the glass superstrate and the NBG perovskite layer and coherent propagation in all other layers. Besides the *nk* data of the perovskite layers, we used the following data: Corning Eagle XG glass[33]; front TCO type "nSCOT" from ANP Corporation,[31] C_{60},[34] SnO_2,[35] intermediate ITO,[19] PEDOT,[36] and copper.[37] In the optical simulations, the SAM is omitted.

The thicknesses of the front TCO, the ITO and the PEDOT:PSS layers were manually varied to get a good match with the experimentally observed interference fringes. The results are shown in **Figure 1**. The thicknesses of all layers are shown in Figure 1b. The simulated absorption of the perovskite layers matches well with the measured EQE. For the NBG perovskite cell, the interference fringes of the simulations are stronger than in the measurements, which might be due to the surface roughness in the experimental APTSC, which is not considered in the simulations. For wavelengths longer than 1000 nm, the simulated reflection strongly overestimates the measured data, indicating that the parasitic absorption in this range is strongly underestimated. This may be caused by neglecting the parasitic plasmonic absorption of a rough copper interface, as discussed in Figure S3b (Supporting Information). The good agreement between the experiment and simulation demonstrates that the selected *nk* data and thicknesses are well suited to perform an optical study on nanotextured all-perovskite tandem solar cells.

3. Simulation Details

Figure 2 illustrates the different texturing schemes investigated in this study: a) a "planar" reference structure; b) a "front-textured" architecture, where the interfaces between the glass superstrate and the wide-bandgap perovskite absorber of the top cell are textured; c) a "front-and-mid-textured" (f-and-m) architecture, in which also the interfaces between the two perovskite absorbers are textured; and d) a "fully textured" architecture. We assume the solar cells to be in "superstrate" configuration, where the solar cell layers are deposited onto a glass substrate through which the incident light reaches the solar cell. When the perovskite layers are prepared via spin-coating or scalable solution-based deposition techniques, the front-textured architecture can be built straightforwardly, while manufacturing the other schemes is more involved (see e.g., Ref. [6]). We also simulated a "back-textured" design, where only the back side of the bottom cell is textured, as illustrated in Figure 2e. Using spin-coating, such a texturing scheme would be feasible in a "substrate" configuration, where the deposition sequence of the subcells would be inverted with no glass on top. However, as this work focuses on the comparison of different texturing schemes, we keep the layer stack unchanged for all schemes.

The optical simulations were performed with the simulation toolbox `JCMsuite`, which rigorously solves Maxwell's equations with the finite element method (FEM)[38] and has been applied successfully for optical simulations of periodically textured solar cells.[5,6,19] **Figure 3a** shows a typical FEM mesh with the layer stack used in this work. The shown front-textured solar cell has sinusoidal hexagonal nanotextures with 750.0 nm period and 202.5 nm texture height, corresponding to a 27% aspect ratio (AR, height-to-period ratio), between glass and the WBG perovskite layer. A hexagonal sinusoidal nanotexture is illustrated in Figure 3b. We performed the simulations for moderate and

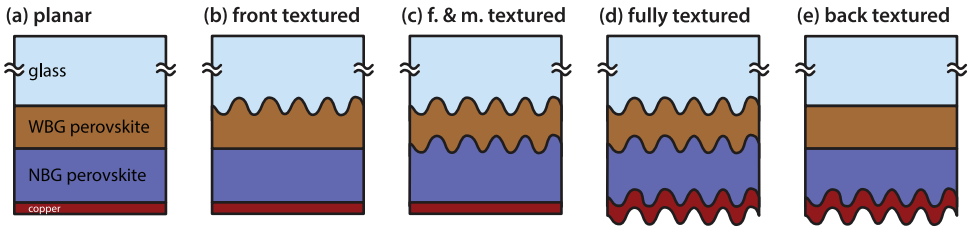

Figure 2. Illustrating the different texturing schemes studied in this work. Note that the layer thicknesses are not to scale and that this illustration does not show a detailed layer structure.

pronounced textures with aspect ratios of 27% and 54%, respectively. The moderate textures are the experimental standard in our lab, but higher aspect ratios are feasible. Because previous work has shown that the aspect ratio affects the optical performance of solar cells much stronger than the period (when the aspect ratio is kept constant),[5] we only looked at one period in this work.

In detail, we performed simulations for vacuum wavelengths λ_0 between 300 and 1190 nm in 10-nm-steps. To get a good balance between accuracy and computational performance, FEM meshes were generated for $\lambda_0 \in [300, 450, 600 \ldots 1050]$ nm, where the 300-nm-mesh was reused for simulations for $\lambda_0 \in [300, 310, 320 \ldots 440]$ nm, and so forth. For each mesh, the maximum side length of the individual elements was restricted to the wavelength in the respective material, λ_0/n. The maximum side length of the elements constituting the sinusoidal interfaces was fixed at 26 nm. The current densities corresponding to the absorption spectra in the different layers were calculated as described in Ref. [39].

4. Glass Correction Algorithm

Light reaches the cell through a 1.1 mm thick glass superstrate. Such thick layers exceed the capabilities of FEM. Therefore, the interaction between light and the air-glass interface atop the solar cell and absorption in the glass superstrate have to be treated after the FEM simulations in a post process. In the FEM simulation, "periodic boundary conditions" are used on the sides and "perfectly matched layers" above and below the unit cell. This means that the glass above the unit cell is treated as infinite halfspace.

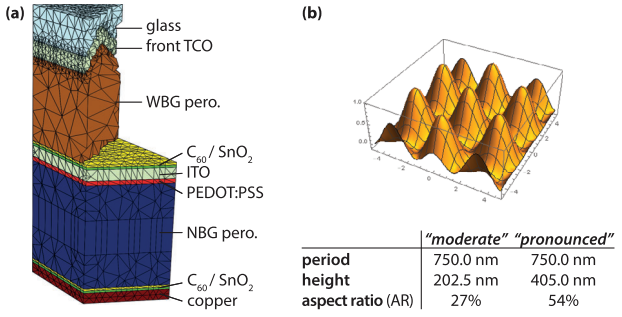

	"moderate"	*"pronounced"*
period	750.0 nm	750.0 nm
height	202.5 nm	405.0 nm
aspect ratio (AR)	27%	54%

Figure 3. a) Layer stack and FEM mesh for the front-textured solar cell with 27% aspect ratio. The self-assembled monolayer, which constitutes the hole-transporting layer in the top cell, is omitted in the optical simulations. b) Illustration of the hexagonal sinusoidal texture and dimensions of the simulated textures.

Often, the air-glass interface on top of the solar cell is only accounted for by correcting for the initial reflection at this interface. In Ref. [40], we have shown that this "zeroth order correction" strongly overestimates reflection of a nanotextured glass-silicon stack. To overcome this issue and model the interactions at the air-glass interface, we developed a rigorous algorithm to correct the reflection of samples with thick glass superstrates: When light enters the solar cell, it interacts with the periodic nanotextures and is scattered into the Bloch family, a well-defined number of directions, which is determined by the (2D) ground shape of the unit cell and the refractive index of the material, into which the light is scattered. Using FEM, the scattering matrix is derived, which couples light incident from all directions of the Bloch family to all outgoing directions. Light reflected into the glass superstrate partially escapes into the air and partially is reflected back into the solar cell. Then, an iterative process is repeated until a pre-defined fraction of the total reflection (here $\leq 10^4$) of the light neither leaves the solar cell nor is absorbed.

For this work, we upgraded the glass-correction algorithm presented in Ref. [40]: first, it now not only treats reflection but also absorption in all layers of the layer stack. Second, we included the absorption in the glass superstrate, which is relevant for short wavelengths. The details on the glass correction are given in Section S1 (Supporting Information).

With the glass correction, we combine coherent propagation of light in the solar cell stack simulated with FEM with incoherent propagation in the glass superstrate. While such a combination of (thin) layers with coherent and (thick) layers with incoherent propagation of light might seem arbitrary at first sight, it often is done for optical simulations of solar cells to account for the coherence properties of sunlight. For example, this approach is also applied in the simulation packages `OPTOS`[41,42] and `GenPro4`.[32]

Figure 4 shows simulation results for the front-textured architecture sketched in Figure 2b with the zeroth-order correction (where only the initial interaction between the incident light and the air-glass interface is accounted for) and the full correction. Because the initially reflected light is partially reflected back into the solar cell and absorbed, the fully corrected reflection is lower than the zeroth-order corrected value.

5. Results

Figure 5a–e shows simulation results for the different texturing schemes sketched in Figure 2. For these simulations, we varied the thickness of the WBG perovskite layer using Newton's method to reach current matching, as in Ref. [43]. All layer thicknesses are the effective layer thicknesses, which is the layer

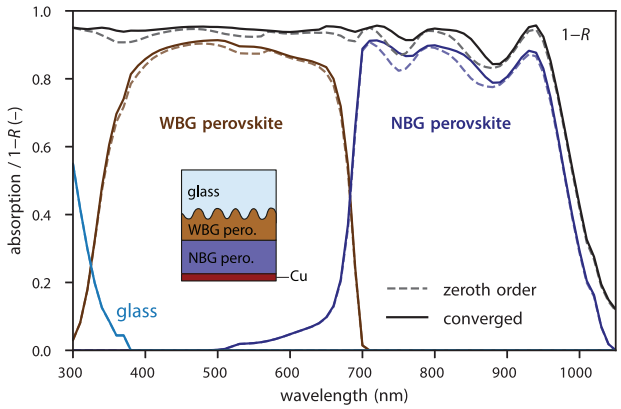

Figure 4. Simulation results for a front-textured device structure with 27% aspect ratio with a zeroth-order correction, where only for the initial interaction of the incident light with the air-glass interface is corrected, and the full correction. The cyan lines show the absorption in the glass superstrate. Details on the glass correction are given in Section S1 (Supporting Information).

thickness of a planar layer with the same volume. This is important for the WBG perovskite layer in the front-textured design and the NBG perovskite layer in the medium- and back-textured designs, where these layers are not conformal. The effective NBG perovskite thickness was kept constant at 1000 nm for all simulations. The resulting WBG perovskite thicknesses and the current densities are shown in Table 1; the current densities are also plotted in Figure 5e.

For the planar architecture, distinct thin-film interferences caused by the TCO layers and the WBG and NBG perovskite absorbers are visible in the absorption profiles and $1 - R$ spectra, in particular at short wavelengths and in the highly absorptive region of the NBG perovskite (750–950 nm). For the "front-textured" architecture, shown in Figure 5a, texturing leads to a better in-coupling of the incident light across all wavelengths. In the NBG perovskite, it decreases the amplitude of the interference fringes; an effect that is stronger for the pronounced texture with 54% AR. The absorption at the absorption edge of the NBG perovskite only increases slightly, which is in line with our observations for perovskite single-junction solar cells.[19] Adding textured interfaces between the two subcells in the "front-and-mid-textured" architecture, shown in Figure 5b, hardly affects the matched current density for 27% aspect ratio, but it strongly increases the current density for 54% aspect ratio leading to the highest value of all simulations, as shown in Figure 5e. For 54% AR the absorption in the NBG perovskite for wavelengths >950 nm wavelength is strongly increased, hence "light trapping" occurs. The results for the "fully textured" architecture are shown in Figure 5c. For the moderate textures (27% AR) this architecture yields the highest current density because it combines in-coupling of light across all wavelengths and light trapping at the absorption edge of the NBG perovskite. For 54% AR, the matched current density is slightly below that of the f-and-m textured architecture. This is likely caused by parasitic absorption in the copper layer, which increases with a higher aspect ratio, as shown in Figure 5f. The increased parasitic absorption in copper likely stems from the excitation of surface plasmons.[44] The last texturing scheme is the "back-textured" architecture shown in Figure 5d. In contrast to the other texturing schemes, here in-coupling of the incident light is not improved. For 27% AR, light trapping for long wavelengths leads to a matched current density comparable to the front-and-f-and-m textured architectures. For 54% AR, light trapping is much weaker because of an increased parasitic absorption in the Cu layer (1.14 mA cm^{-2} for 54% AR; 0.69 mA cm^{-2} for 27% AR), similar as for the "fully textured" case. Because of the parasitic absorption in Cu, the back-textured architecture yields the lowest matched current density of all investigated architectures with pronounced textures (54% AR). Figure S4 (Supporting Information) shows the parasitic absorption in copper for all texturing schemes: the parasitic absorption is mainly affected by textures between the NBG perovskite layer and the Cu back contact.

Table 1. Simulation results for the different architectures sketched in Figure 2. For each architecture, the effective absorber thickness d_{WBG} of the wide-bandgap top cell and the current densities J_{WBG} and J_{NBG} for the two subcells are shown.

architecture	aspect ratio 27%			aspect ratio 54%		
	d_{WBG} (nm)	J_{WBG} (mA cm^{-2})	J_{NBG}	d_{WBG} (nm)	J_{WBG} (mA cm^{-2})	J_{NBG}
planar	765	16.17	16.17	765	16.17	16.17
front	764	16.59	16.58	735	16.92	16.94
front and mid	797	16.61	16.60	916	17.16	17.13
full	931	16.93	16.94	877	17.07	17.06
back	976	16.62	16.61	843	16.36	16.37

Figure 6a shows the absorption profiles for the planar device architecture. Here, 79% of the photons available from the solar spectrum between 300 and 1050 nm are utilized by the perovskite layers, while 15% are lost via reflection. Other significant losses are parasitic absorption in the front TCO, the intermediate ITO and PEDOT:PSS layers and the copper back contact. Figure 6b shows the front and mid-textured architecture with 54% aspect ratio, which yielded the highest current densities. Here, 84% of the photons available from the solar spectrum between 300 and 1050 nm are utilized by the perovskite layers, while 8% are lost via reflection. While the loss at the front TCO is comparable to the planar case, the parasitic absorption in the intermediate ITO and PEDOT:PSS layers and the copper back contact is increased. Hence, texturing not only leads to light trapping in the NBG perovskite, but also in the supporting layers.

6. Discussion and Outlook

We tested numerically how textures at different locations of all-perovskite tandem solar cells (APTSCs) affect their optical performance. Texturing at the front, between the glass superstrate and the WBG perovskite top cell has an antireflective effect across the whole wavelength region. Texturing between the WBG perovskite top cell and the NBG perovskite bottom cell has no additional effect for a moderate texture (27% aspect ratio) but leads to light trapping in the NBG perovskite for the pronounced texture (54% aspect ratio). Moderate texturing at the

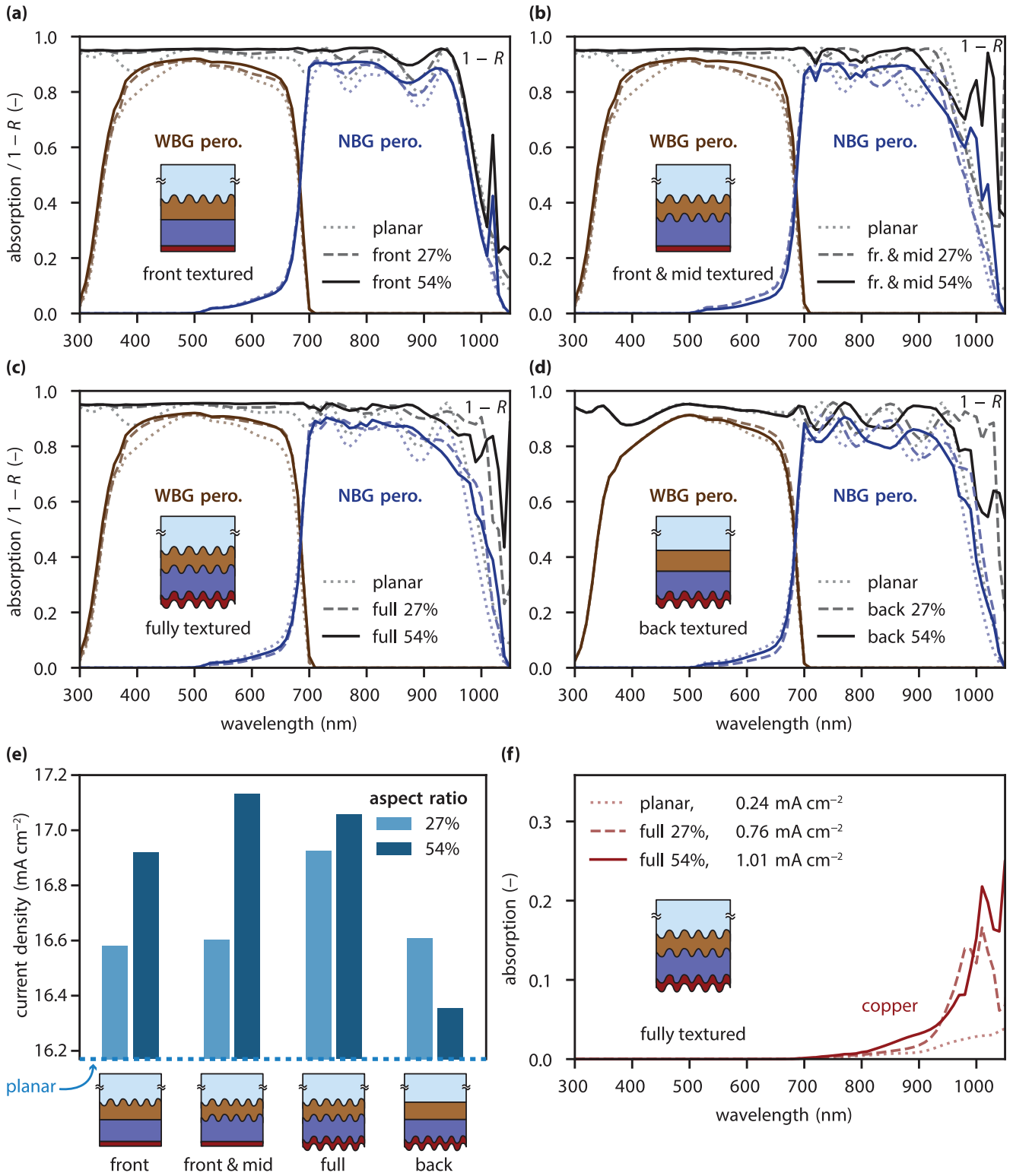

Figure 5. Simulation results for a) front-side textured solar cells, b)front-and-mid-textured solar cell, c) fully textured solar cells, and d) back-textured solar cells as illustrated in Figure 2. All results are shown for moderate (27% aspect ratio) and pronounced (54% aspect ratio) textures. In all subfigures, results for a planar solar cell are shown as a reference. For these simulations, we varied the thickness of the WBG perovskite layer using Newton's method to reach current matching, as in Ref. [43]. e) Matched current densities for the different architectures, determined as $\min(J_{WBG}, J_{NBG})$ from the values shown in **Table 1**. The blue dashed baseline corresponds to the planar reference. f) Parasitic absorption in copper for fully textured solar cells. The corresponding current densities are shown in the legend.

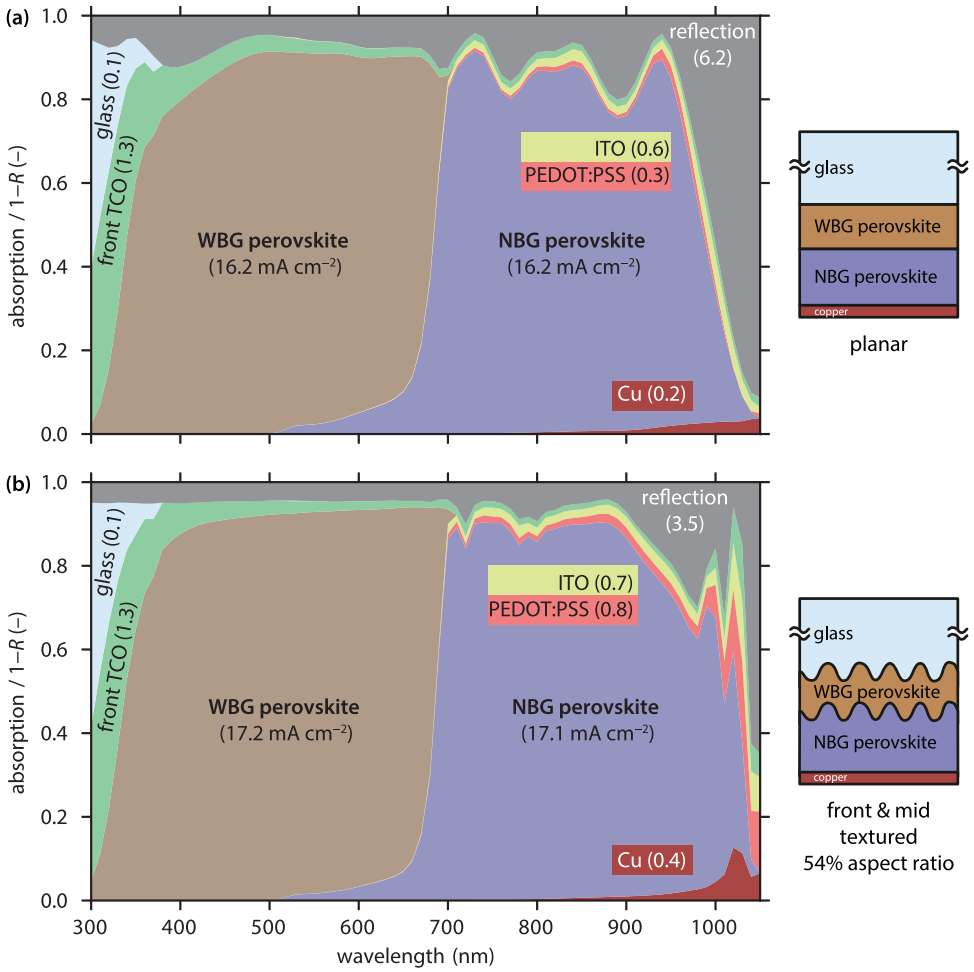

Figure 6. Absorption profiles for the a) planar device architecture and the b) front and mid-textured architecture with 54% aspect ratio, which yielded the highest current densities in the perovskite layers. The number in brackets denotes the corresponding current densities. The C_{60} and SnO_2 layers are not shown because their absorption losses are negligible.

back, between the NBG perovskite absorber and the copper back contact, leads to light trapping in the NBG perovskite but also excites surface plasmons in the Cu layer. For a pronounced texture at the back, the parasitic absorption losses in Cu are so large that they hamper light trapping in the NBG perovskite. Texturing potentially enables matched current densities beyond 17 mA cm^{-2}, which significantly exceeds recent experimentally achieved values of 16.0 mA cm^{-2},[45] 16.1[30] and 16.5 mA cm^{-2}.[14] The front- and back-textured architectures can be fabricated in super- and substrate processing, respectively, with spin-coating. For a fully textured design, usually the perovskites need to be processed with other deposition methods, such as evaporation.

To further improve APTSCs from an optical point of view, several measures can be taken: The overall reflection can be further reduced by applying an antireflective coating on top of the glass superstrate. The losses in the ITO recombination layer can be reduced by reducing its thickness. Further, PEDOT:PSS, which is the hole transport layer for the bottom cell, can be replaced by a self-assembled monolayer, as for the top cell.[46]

To reduce the parasitic absorption in the rear metal, silicon solar cells typically employ antireflective layers between the absorber and metal to reduce the excitation of surface plasmons in the metal.[31,44] **Figure 7** shows the effect of antireflective interlayers made of ITO and silicon oxide SiO_x in between the copper back contact and the SnO_2 hole transport layer of the bottom cell. For the first test, we set the thickness of these layers to 150 nm. The ITO interlayer with the same composition as the ITO recombination layer reduces the Cu absorption from 1.01 to 0.70 mA cm^{-2}. However, the ITO layer absorbs 0.91 mA cm^{-2}, leading to an overall increased parasitic absorption and consequently a reduced current density in the NBG perovskite. A transparent SiO_x interlayer ($n \approx 1.45$) reduces the Cu absorption from 1.01 to 0.42 mA cm^{-2}, leading to an increased current density in the NBG perovskite. If the WBG perovskite thickness was adapted such that the additional current was distributed evenly between the WBG and NBG perovskites, the matched current density would be 17.18 mA cm^{-2}; slightly higher than for the pronounced f-and-m textured device. However, SiO_x is an insulating material. Therefore, more involved contacting schemes at the back would be required.[31]

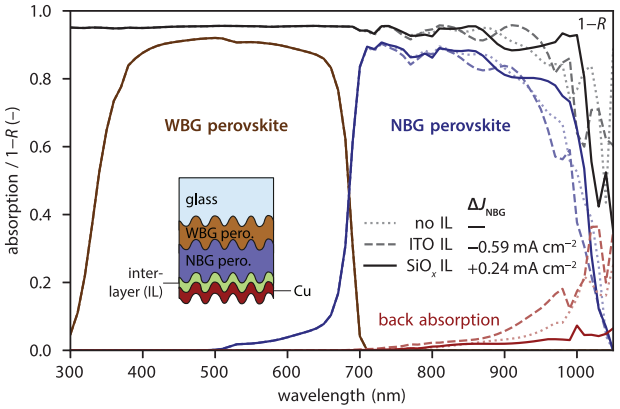

Figure 7. Simulation results for a fully textured solar cell sketched in Figure 2d with 54% aspect ratio and three different layer stacks at the back: $C_{60}/SnO_2/Cu$ (no interlayer, IL), a 150 nm ITO IL between SnO_2 and Cu, and a 150 nm SiO_x IL between SnO_2 and Cu. The change in current density in the NBG perovskite with respect to the case with no IL (ΔJ_{NBG}) is given. "Back absorption" denotes the absorption in copper and—if applicable—the ITO layer. C_{60}, SnO_2 and SiO_x do not absorb in the relevant wavelength range.

Supporting Information

Supporting Information is available from the Wiley Online Library or from the author.

Acknowledgements

The results were obtained at the Berlin Joint Lab for Optical Simulations for Energy Research (BerOSE) of Helmholtz-Zentrum Berlin für Materialien und Energie, Zuse-Institut Berlin, and Freie Universität Berlin. Funding was provided by the German Federal Ministry of Education and Research (BMBF) through the project PEROWIN (grant no. 03SF0631), by the Helmholtz Association within the project HySPRINT Innovation Lab, and from the European Union's Horizon 2020 Programme under grant agreement number 101075605 (SuPerTandem). The authors further acknowledge HyPerCells, a joint graduate school of the University of Potsdam and the Helmholtz-Zentrum Berlin für Materialien und Energie.

Open access funding enabled and organized by Projekt DEAL.

Conflict of Interest

The authors declare no conflict of interest.

Data Availability Statement

The data that support the findings of this study are available from the corresponding author upon reasonable request.

Keywords

all-perovskite tandem solar cells, ellipsometry, optical simulations, photovoltaics

Received: August 29, 2024
Published online: September 24, 2024

[1] IPCC, in, *Climate Change 2023: Synthesis Report*, (Eds.: Core Writing Team, H. Lee, J. Romero), IPCC, Geneva, Switzerland, **2023**, pp. 1–34.
[2] A. Richter, M. Hermle, S. Glunz, *IEEE J. Photovolt.* **2013**, *3*, 1184.
[3] 34.6%! Record-breaker LONGi Once Again Sets a New World Efficiency for Silicon-perovskite Tandem Solar Cells, **2024**, https://www.longi.com/en/news/2024-snec-silicon-perovskite-tandem-solar-cells-new-world-efficiency/ (accessed: 28 August 2024).
[4] M. Jošt, E. Köhnen, A. B. Morales-Vilches, B. Lipovšek, K. Jäger, B. Macco, A. Al-Ashouri, J. Krč, L. Korte, B. Rech, R. Schlatmann, M. Topič, B. Stannowski, S. Albrecht, *Energy Environ. Sci.* **2018**, *11*, 3511.
[5] K. Jäger, J. Sutter, M. Hammerschmidt, P.-I. Schneider, C. Becker, *Nanophotonics* **2021**, *10*, 1991.
[6] P. Tockhorn, J. Sutter, A. Cruz, P. Wagner, K. Jäger, D. Yoo, F. Lang, M. Grischek, B. Li, J. Li, O. Shargaieva, E. Unger, A. Al-Ashouri, E. Köhnen, M. Stolterfoht, D. Neher, R. Schlatmann, B. Rech, B. Stannowski, S. Albrecht, C. Becker, *Nat. Nanotechnol.* **2022**, *17*, 1214.
[7] M. De Bastiani, R. Jalmood, J. Liu, C. Ossig, A. Vlk, K. Vegso, M. Babics, F. H. Isikgor, A. S. Selvin, R. Azmi, E. Ugur, S. Banerjee, A. J. Mirabelli, E. Aydin, T. G. Allen, A. Ur Rehman, E. Van Kerschaver, P. Siffalovic, M. E. Stuckelberger, M. Ledinsky, S. De Wolf, *Adv. Funct. Mater.* **2022**, *33*, 4.
[8] X. Y. Chin, D. Turkay, J. A. Steele, S. Tabean, S. Eswara, M. Mensi, P. Fiala, C. M. Wolff, A. Paracchino, K. Artuk, D. Jacobs, Q. Guesnay, F. Sahli, G. Andreatta, M. Boccard, Q. Jeangros, C. Ballif, *Science* **2023**, *381*, 59.
[9] X. Wu, B. Li, Z. Zhu, C.-C. Chueh, A. K.-Y. Jen, *Chem. Soc. Rev.* **2021**, *50*, 13090.
[10] Q.-Q. Chu, Z. Sun, J. Hah, K.-s. Moon, B. Cheng, D. Wang, P. Xiao, Y. Zhou, A. Petrozza, G.-J. Yang, H. Wang, C.-P. Wong, *Mater. Today* **2023**, *67*, 399.
[11] N. Bartie, L. Cobos-Becerra, F. Mathies, J. Dagar, E. Unger, M. Fröhling, M. A. Reuter, R. Schlatmann, *J. Ind. Ecol.* **2023**, *27*, 993.
[12] C. Li, L. Chen, F. Jiang, Z. Song, X. Wang, A. Balvanz, E. Ugur, Y. Liu, C. Liu, A. Maxwell, H. Chen, Y. Liu, Z. Wang, P. Xia, Y. Li, S. Fu, N. Sun, C. R. Grice, X. Wu, Z. Fink, Q. Hu, L. Zeng, E. Jung, J. Wang, S. M. Park, D. Luo, C. Chen, J. Shen, Y. Han, C. A. R. Perini, et al., *Nat. Energy* **2024**, 1 https://doi.org/10.1038/s41560-024-01613-8.
[13] M. A. Green, E. D. Dunlop, M. Yoshita, N. Kopidakis, K. Bothe, G. Siefer, X. Hao, *Prog.Photovolt.: Res. Appl.* **2023**, *32*, 3.
[14] R. Lin, Y. Wang, Q. Lu, B. Tang, J. Li, H. Gao, Y. Gao, H. Li, C. Ding, J. Wen, P. Wu, C. Liu, S. Zhao, K. Xiao, Z. Liu, C. Ma, Y. Deng, L. Li, F. Fan, H. Tan, *Nature* **2023**, *620*, 994.
[15] G. E. Eperon, T. Leijtens, K. A. Bush, R. Prasanna, T. Green, J. T.-W. Wang, D. P. McMeekin, G. Volonakis, R. L. Milot, R. May, A. Palmstrom, D. J. Slotcavage, R. A. Belisle, J. B. Patel, E. S. Parrott, R. J. Sutton, W. Ma, F. Moghadam, B. Conings, A. Babayigit, H.-G. Boyen, S. Bent, F. Giustino, L. M. Herz, M. B. Johnston, M. D. McGehee, H. J. Snaith, *Science* **2016**, *354*, 861.
[16] M. Moradbeigi, M. Razaghi, *Sci. Rep.* **2022**, *12*, 6733.
[17] B. Chen, Z. Yu, A. Onno, Z. Yu, S. Chen, J. Wang, Z. C. Holman, J. Huang, *Sci. Adv.* **2022**, *8*, eadd0377.
[18] Z. Yu, J. Wang, B. Chen, M. A. Uddin, Z. Ni, G. Yang, J. Huang, *Adv. Mater.* **2022**, *34*, 2205769.
[19] P. Tockhorn, J. Sutter, R. Colom, L. Kegelmann, A. Al-Ashouri, M. Roß, K. Jäger, T. Unold, S. Burger, S. Albrecht, C. Becker, *ACS Photonics* **2020**, *7*, 2589.
[20] The term *superstrate* denotes a substrate located on the front side of the solar cell such that the incident light passes the superstrate before it reaches the other layers of the solar cell.
[21] M. Anaya, J. P. Correa-Baena, G. Lozano, M. Saliba, P. Anguita, B. Roose, A. Abate, U. Steiner, M. Grätzel, M. E. Calvo, A. Hagfeldt, H. Míguez, *J. Mater. Chem.A* **2016**, *4*, 11214.

[22] M. T. Hörantner, T. Leijtens, M. E. Ziffer, G. E. Eperon, M. G. Christoforo, M. D. McGehee, H. J. Snaith, *ACS Energy Lett.* **2017**, *2*, 2506.
[23] K. Xiao, R. Lin, Q. Han, Y. Hou, Z. Qin, H. T. Nguyen, J. Wen, M. Wei, V. Yeddu, M. I. Saidaminov, Y. Gao, X. Luo, Y. Wang, H. Gao, C. Zhang, J. Xu, J. Zhu, E. H. Sargent, H. Tan, *Nat. Energy* **2020**, *5*, 870.
[24] A. R. Bowman, F. Lang, Y.-H. Chiang, A. Jiménez-Solano, K. Frohna, G. E. Eperon, E. Ruggeri, M. Abdi-Jalebi, M. Anaya, B. V. Lotsch, S. D. Stranks, *ACS Energy Lett.* **2021**, 612.
[25] A. Filippetti, S. Kahmann, C. Caddeo, A. Mattoni, M. Saba, A. Bosin, M. A. Loi, *J. Mater. Chem.A* **2021**, *9*, 11812.
[26] H. Fujiwara, *Spectroscopic Ellipsometry: Principles and Applications*, Wiley, Hoboken, New Jersey **2007**.
[27] G. E. Jellison, F. A. Modine, *Appl. Phys. Lett.* **1996**, *69*, 371.
[28] G. E. Jellison, F. A. Modine, *Appl. Phys. Lett.* **1996**, *69*, 2137.
[29] H. Fujiwara, *Effect of Roughness on Ellipsometry Analysis*, Springer International Publishing, New York **2018**, pp. 155–172.
[30] F. Yang, P. Tockhorn, A. Musiienko, F. Lang, D. Menzel, R. Macqueen, E. Köhnen, K. Xu, S. Mariotti, D. Mantione, L. Merten, A. Hinderhofer, B. Li, D. R. Wargulski, S. P. Harvey, J. Zhang, F. Scheler, S. Berwig, M. Roß, J. Thiesbrummel, A. Al-Ashouri, K. O. Brinkmann, T. Riedl, F. Schreiber, D. Abou-Ras, H. Snaith, D. Neher, L. Korte, M. Stolterfoht, S. Albrecht, *Adv. Mater.* **2023**, *36*, 2307743.
[31] A. Cruz, D. Erfurt, P. Wagner, A. B. Morales-Vilches, F. Ruske, R. Schlatmann, B. Stannowski, *Sol. Energ. Mat. Sol. C.* **2022**, *236*, 111493.
[32] R. Santbergen, T. Meguro, T. Suezaki, G. Koizumi, K. Yamamoto, M. Zeman, *IEEE J. Photovolt.* **2017**, *7*, 919.
[33] C. V. Cushman, B. A. Sturgell, A. C. Martin, B. M. Lunt, N. J. Smith, M. R. Linford, *Surf. Sci. Spectra* **2016**, *23*, 55.
[34] D. Menzel, A. Al-Ashouri, A. Tejada, I. Levine, J. A. Guerra, B. Rech, S. Albrecht, L. Korte, *Adv. Energy Mater.* **2022**, *12*, 2201109.
[35] E. Köhnen, M. Jošt, A. B. Morales-Vilches, P. Tockhorn, A. Al-Ashouri, B. Macco, L. Kegelmann, L. Korte, B. Rech, R. Schlatmann, B. Stannowski, S. Albrecht, *Sustainable Energy Fuels* **2019**, *3*, 1995.
[36] C.-W. Chen, S.-Y. Hsiao, C.-Y. Chen, H.-W. Kang, Z.-Y. Huang, H.-W. Lin, *J. Mater. Chem.A* **2015**, *3*, 9152.
[37] P. B. Johnson, R. W. Christy, *Phys. Rev. B* **1972**, *6*, 4370.
[38] J. Pomplun, S. Burger, L. Zschiedrich, F. Schmidt, *Phys. Status Solidi B* **2007**, *244*, 3419.
[39] K. Jäger, C. Barth, M. Hammerschmidt, S. Herrmann, S. Burger, F. Schmidt, C. Becker, *Opt. Express* **2016**, *24*, A569.
[40] K. Jäger, G. Köppel, M. Hammerschmidt, S. Burger, C. Becker, *Opt. Express* **2018**, *26*, A99.
[41] J. Eisenlohr, N. Tucher, O. Höhn, H. Hauser, M. Peters, P. Kiefel, J. C. Goldschmidt, B. Bläsi, *Opt. Express* **2015**, *23*, A502.
[42] N. Tucher, O. Höhn, J. C. Goldschmidt, B. Bläsi, *Opt. Express* **2018**, *26*, A761.
[43] D. Chen, P. Manley, P. Tockhorn, D. Eisenhauer, G. Köppel, M. Hammerschmidt, S. Burger, S. Albrecht, C. Becker, K. Jäger, *J. Photonics Energy* **2018**, *8*, 022601.
[44] Z. C. Holman, M. Filipič, A. Descoeudres, S. De Wolf, F. Smole, M. Topič, C. Ballif, *J. Appl. Phys.* **2013**, *113*, 013107.
[45] S. Zhou, S. Fu, C. Wang, W. Meng, J. Zhou, Y. Zou, Q. Lin, L. Huang, W. Zhang, G. Zeng, D. Pu, H. Guan, C. Wang, K. Dong, H. Cui, S. Wang, T. Wang, G. Fang, W. Ke, *Nature* **2023**, *624*, 69.
[46] C. Liu, R. Lin, Y. Wang, H. Gao, P. Wu, H. Luo, X. Zheng, B. Tang, Z. Huang, H. Sun, S. Zhao, Y. Guo, J. Wen, F. Fan, H. Tan, *Angew. Chem. Int. Ed.* **2023**, *62*, e202313374.